C.T. Campana, G. Merisio, F. Topputo
Exterior Earth Moon Transfers Design Using the Theory of Functional Connections and Homotopy
in: AIAA Scitech 2024 Forum, AIAA, 2024, ISBN: 9781624107115, p. 1-15, AIAA 2024-0207
[AIAA Scitech 2024 Forum, Orlando, FL, USA, 8-12 Jan. 2024]
doi:10.2514/6.2024-0207

Exterior Earth–Moon Transfers Design Using the Theory of Functional Connections and Homotopy

Claudio Toquinho Campana*, Gianmario Merisio†, and Francesco Topputo‡
Politecnico di Milano, Via La Masa 34, Milano, 20156, Italy

Cost-effective access to the lunar environment can be achieved by leveraging the weak stability boundary of the Earth–Moon–Sun system. Upcoming missions to our natural satellite are foreseen to exploit these long-duration transfers. By combining the recent Theory of Functional Connection and a homotopy continuation process, this paper proposes a novel method to design low-energy transfers to the Moon. Planar patched transfer legs within the Earth–Moon and the Sun–Earth systems are refined into higher-fidelity models. Eventually, the full Earth–Moon transfer conforms to the dynamics of the planar Earth–Moon Sun-perturbed, bi-circular restricted four-body problem. This method eliminates the need to numerically propagate the dynamic equations during the continuation and final convergence to the full trajectory. A grid search is implemented to generate a wide range of exterior Earth–Moon transfers. This work illustrates that the Theory of Functional Connections can effectively represent two-impulses, long-duration, low-energy transfers modeled in chaotic dynamic environments. Furthermore, its synergy with a homotopic continuation approach is demonstrated.

I. Introduction

In the recent years, space exploration is experiencing a flourishing growth. The human interest in pushing the boundaries beyond the Earth is fueling scientific progress in all fields related to astronautics. The exploration and utilization of the lunar environment represent the initial strides toward human settlement on other celestial bodies. Recently, several missions have been launched in the cislunar space (CAPSTONE [1], ArgoMoon [2], EQUULEUS [3]) and many others are planned for the near future (LUMIO [4], Chang'e-6 *). On the wave of this renewed interest in our natural satellite, the ambitious ARTEMIS program [5] aspires to develop the technologies necessary to establish permanent lunar outposts both on the Moon surface and in the cislunar space. The success of this program would set an important milestone in the human presence in space. In this context, the development of new techniques for mission design and trajectory optimization in chaotic environments is of paramount importance to further enhance the overall appeal of space exploration.

The dynamics governing the motion of a spacecraft in an interplanetary cruise is intrinsically chaotic [6]. Multiple attractors and perturbations act together, thereby making the phase space extremely sensitive to small variations in the spacecraft states and rather complex to characterize. Therefore, the design of trajectories in such environments is especially difficult. On the other hand, this complexity enriches the phase space, thereby permitting to design preliminary cost-effective transfer guesses that exploit dynamic structures arising from simplified models. Periodic orbits [7] and invariant manifolds [6] are some examples. Overall, trajectories designed in these models enable for safer and more fuel-efficient transfers, this usually at the expenses of longer travel times [8].

In this work, a novel approach to design two-impulse, long-duration, low-energy trajectories is proposed. A technique for effective Earth–Moon exterior trajectories prototyping and design in intricate and chaotic dynamic regimes is developed. Firstly, a seeding trajectory composed of a departure leg from the Earth and an arrival one to the Moon is constructed. Dynamic structures are exploited similarly to what practiced in [9]. The Theory of Functional Connections (TFC) [10] is subsequently adopted to analytically approximate the two legs. A homotopic continuation procedure [11] is implemented to gradually refine the legs into more realistic dynamic models. Eventually, a full Earth–Moon transfer trajectory is achieved. This procedure circumvents the need for repeatedly performing numerical integration of the dynamic equations within a shooting framework, thereby facilitating the overall design process. A grid search is implemented to generate numerous admissible exterior transfers.

*PhD Student, Dept. of Aerospace Science and Technology, claudiotoquinho.campana@polimi.it
†PostDoctoral Research Fellow, Dept. of Aerospace Science and Technology
‡Professor, Dept. of Aerospace Science and Technology
*https://www.planetary.org/space-missions/change-6-collecting-the-first-lunar-farside-samples

Table 1 Physical parameters of the Sun–Earth and Earth–Moon CR3BPs.

Symbol	Value		Units	Description
	Sun–Earth	Earth–Moon		
μ	$3.003\,480 \times 10^{-6}$	$1.215\,066 \times 10^{-2}$	-	Mass parameter
DU	$1.494\,609 \times 10^{8}$	$3.844\,050 \times 10^{5}$	km	Distance unit
TU	$5.812\,673 \times 10^{1}$	4.348 113	days	Time unit
VU	$2.976\,035 \times 10^{1}$	1.023 232	km/s	Speed unit

The paper is structured as follows. In Sec. II the dynamic models and the theoretical fundamentals of the tools employed are presented. Section III describes the method and the trajectory design approach. Two-impulse, exterior Earth–Moon transfers are generated in Sec. IV following the devised method. Eventually, Sec. V summarizes the contributions of this study.

II. Background

A. Dynamic models

1. Planar circular restricted three-body problem

In the planar Circular Restricted Three-Body Problem (CR3BP), two attractors P_1 and P_2 of masses $M_1 > M_2$ revolve in circular orbits about their common barycentre. The motion of a third body P_3 of negligible mass, representing the spacecraft, is governed by the gravitational pull of the primaries. Denoting with $\mu = M_2/(M_1 + M_2)$ the normalized gravitational parameter, the motion of P_3 can be represented in a convenient (x, y) rotating frame (rf) with the origin at the centre of mass of the primaries and the x axis pointing towards P_2. The dynamic equations governing the motion of P_3 are formulated in normalized mass, distance, and time units as [12]

$$\ddot{x} = 2\dot{y} + \frac{\partial \Omega_3}{\partial x}, \quad \ddot{y} = -2\dot{x} + \frac{\partial \Omega_3}{\partial y}, \tag{1}$$

where the effective potential Ω_3 is

$$\Omega_3(x, y) = \frac{1}{2}(x^2 + y^2) + \frac{1-\mu}{r_1} + \frac{\mu}{r_2} + \frac{1}{2}\mu(1-\mu). \tag{2}$$

The distance of the spacecraft from P_1, located at $(-\mu, 0)$, is $r_1 = [(x+\mu)^2 + y^2]^{1/2}$, whereas the distance from P_2, located at $(1-\mu, 0)$, is $r_2 = [(x+\mu-1)^2 + y^2]^{1/2}$. The dynamics gives rise to five equilibria, known as Lagrange points L_i, $i = 1, \ldots, 5$. The autonomous dynamics enables an integral of motion, the Jacobi constant, which is equal to [12]

$$J(x, y, \dot{x}, \dot{y}) = 2\Omega_3(x, y) - (\dot{x}^2 + \dot{y}^2). \tag{3}$$

Depending on the value of the Jacobi constant, the spacecraft may or may not transit through specific areas in the configuration space, the boundaries of which delimit Hill's region. Table 1 reports the physical constants used in this work, both for the Sun–Earth (SE) and the Earth–Moon (EM) CR3BPs. The units of distance, time, and speed are used to map scaled quantities into physical units.

2. Planar Sun–Earth Moon-perturbed bi-circular restricted four-body problem

The planar Sun–Earth Moon-perturbed Bi-Circular Restricted Four-Body Problem (SE-BCR4BP) introduces the perturbation of the Moon, which is revolving in a circular orbit about the Earth, into the SE-CR3BP. Referring to Fig. 1, the dynamic equations expressed in the (x, y) rotating system of reference are formulated as [13]

$$\ddot{x} = 2\dot{y} + \frac{\partial \Omega_4^{\mathrm{SE}}}{\partial x}, \quad \ddot{y} = -2\dot{x} + \frac{\partial \Omega_4^{\mathrm{SE}}}{\partial y}, \tag{4}$$

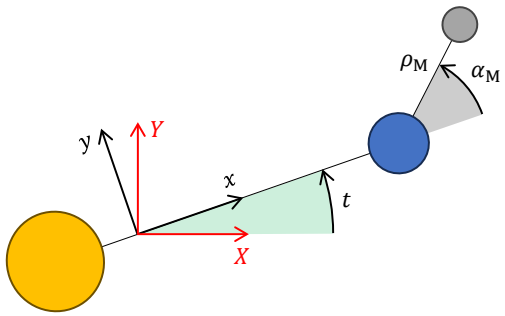

Fig. 1 SE-BCR4BP model (not to scale). Sun in yellow, Earth in blue, Moon in gray.

Table 2 Physical parameters of the SE-BCR4BP.

Symbol	Value	Units	Description
m_M	$3.694\,317 \times 10^{-8}$	-	Scaled Moon mass
ρ_M	$2.571\,942 \times 10^{-3}$	-	Scaled Earth–Moon distance
ω_M	$1.236\,826 \times 10^{1}$	-	Scaled Moon angular velocity

where the new effective potential can be calculated starting from Eq. (2). Hence,

$$\Omega_4^{SE}(x, y, t) = \Omega_3^{SE}(x, y) + \frac{m_M}{r_3(t)}. \tag{5}$$

The mass of the Moon is scaled with respect to the units of the SE-CR3BP (m_M) and its distance from the spacecraft is

$$r_3(t) = \left[\left(x + \mu_{SE} - 1 - \rho_M \cos(\alpha_M(t))\right)^2 + \left(y - \rho_M \sin(\alpha_M(t))\right)^2\right]^{1/2}, \tag{6}$$

where ρ_M is the scaled Earth–Moon distance. A time dependence makes the model non-autonomous. The synodic frame is rotated with respect to the inertial reference (X, Y) by an angle t, non-dimensional time parameter of the Sun–Earth system. The Moon phase angle $\alpha_M(t)$ is calculated as

$$\alpha_M(t) = \omega_M(t - t^{ref}) + \alpha_M^{ref}, \tag{7}$$

where ω_M is the Moon angular velocity relative to the Sun–Earth rotating frame. The initial phase of the Moon equals α_M^{ref} at the reference time t^{ref}. The parameters of this model are shown in Table 2. A scaling with respect to the reference values of the SE-CR3BP is adopted.

3. Planar Earth–Moon Sun-perturbed bi-circular restricted four-body problem

In the planar Earth–Moon Sun-perturbed Bi-Circular Restricted Four-Body Problem (EM-BCR4BP) the Sun revolves in a circular orbit about the center of mass of the Earth–Moon system. Referring to Fig. 2, the dynamic equations in the (x, y) rotating reference frame are formulated by incorporating the Sun in the EM-CR3BP as [14]

$$\ddot{x} = 2\dot{y} + \frac{\partial \Omega_4^{EM}}{\partial x}, \quad \ddot{y} = -2\dot{x} + \frac{\partial \Omega_4^{EM}}{\partial y}, \tag{8}$$

where

$$\Omega_4^{EM}(x, y, t) = \Omega_3^{EM}(x, y) + \frac{m_S}{r_3(t)} - \frac{m_S}{\rho_S^2}\left(x \cos(\alpha_S(t)) + y \sin(\alpha_S(t))\right). \tag{9}$$

In the equation, m_S and ρ_S represent the mass of the Sun and its distance from the Earth–Moon barycentre respectively, scaled with respect to the values of the EM-CR3BP. The distance of the spacecraft from the Sun is

$$r_3(t) = \left[\left(x - \rho_S \cos(\alpha_S(t))\right)^2 + \left(y - \rho_S \sin(\alpha_S(t))\right)^2\right]^{1/2}. \tag{10}$$

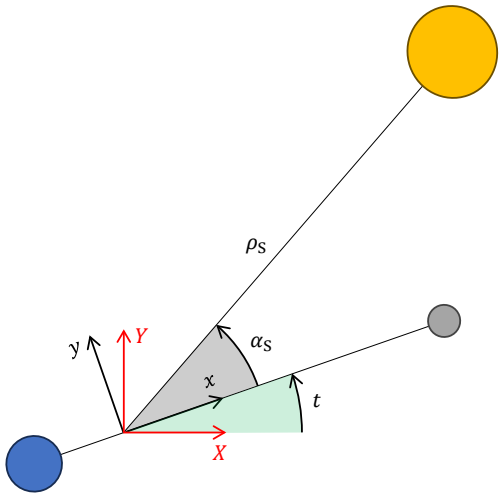

Fig. 2 EM-BCR4BP model (not to scale). Sun in yellow, Earth in blue, Moon in gray.

Table 3 Physical parameters of the EM-BCR4BP.

Symbol	Value	Units	Description
m_S	$3.289\,005 \times 10^{5}$	-	Scaled Sun mass
ρ_S	$3.888\,111 \times 10^{2}$	-	Scaled (Earth+Moon)–Sun distance
ω_S	$-9.251\,959 \times 10^{-1}$	-	Scaled Sun angular velocity

The synodic frame is rotated with respect to a non-rotating one (X, Y) by t, in this case representing the non-dimensional time parameter of the Earth–Moon system. Furthermore, the time dependence t makes this dynamic model non-autonomous. The phase angle $\alpha_S(t)$ in the Earth–Moon rotating frame is expressed as

$$\alpha_S(t) = \omega_S(t - t^{\text{ref}}) + \alpha_S^{\text{ref}}, \tag{11}$$

where ω_S is the relative Sun angular velocity and α_S^{ref} is its phase angle at the reference time t^{ref}. Table 3 reports the scaled parameters of this model.

B. Theory of Functional Connections

The TFC provides a useful formulation to express *all* possible functions satisfying certain constraints [10]. This is achieved by analytically embedding a set of k linear constraints in a functional constructed as linear combination of some basis functions. This makes the underlying principle of the TFC closely related to spectral methods for functional interpolation [15]. Several works adopted the TFC to solve mathematical problems such as approximation of solutions of differential equations [16–18]. Some authors used the TFC to solve astrodynamic problems as well [19, 20].

In general, the TFC functional $x(t, g_x(t))$ satisfying a set of k linear constraints can be formulated as [19]

$$x(t, g_x(t)) = g_x(t) + \sum_{j=1}^{k} \phi_j(t)\, \rho_j(t, g_x(t)), \tag{12}$$

where $g_x(t)$ is a free function, $\phi_j(t)$ are the switching functions, and $\rho_j(t, g_x(t))$ are the projection functionals enforcing the constraints. The free function is a linear combination of m basis functions. In this work, Chebyshev polynomials of the first kind ($\boldsymbol{h}(z(t)) \in \mathbb{R}^m$) are adopted. A mapping between the domain of definition of the Chebyshev polynomials ($z \in [z_0, z_f]$, $z_0 = -1$ and $z_f = 1$) and the time domain is necessary [17]. Considering $\boldsymbol{\xi}_x \in \mathbb{R}^m$ to be the vector of coefficients that must be estimated to perform the functional interpolation, it results that $g_x(t) = \boldsymbol{h}(z(t))^\top \boldsymbol{\xi}_x$. The switching functions are expressed as $\phi_j(t) = s_i(t)\alpha_{ij}$ where k linearly independent supporting functions $s_i(t)$ are

multiplied by α_{ij} coefficients. The switching functions are active, i.e., equal to 1, only when the respective constraints must be enforced. Simultaneously, the remaining inactive switching functions equal 0.

In this study, a TFC formulation represents the solution of a two-point boundary value problem. Two functionals are needed to approximate the time evolution of the states $x(t)$ and $y(t)$ of the spacecraft, with fixed initial and final positions at times t_0 and t_f respectively. Two supporting functions $s_i(t) = t^{i-1}$, for $i = 1, 2$, are introduced to derive the switching functions $\phi_j(t) = \alpha_{1j} + t\,\alpha_{2j}$ such that

$$\begin{aligned} \phi_1(t_0) &= 1, \quad \phi_1(t_\mathrm{f}) = 0; \\ \phi_2(t_0) &= 0, \quad \phi_2(t_\mathrm{f}) = 1. \end{aligned} \tag{13}$$

From this set of conditions, the switching functions can be derived and they result to be

$$\phi_1(t) = \frac{t_\mathrm{f} - t}{t_\mathrm{f} - t_0} \quad \text{and} \quad \phi_2(t) = \frac{t - t_0}{t_\mathrm{f} - t_0}. \tag{14}$$

Finally, Eq. (12) is specialized for the two-point boundary value problem leading to

$$x(t, g_x(t)) = g_x(t) + \frac{t_\mathrm{f} - t}{t_\mathrm{f} - t_0}(x_0 - g_x(t_0)) + \frac{t - t_0}{t_\mathrm{f} - t_0}(x_\mathrm{f} - g_x(t_\mathrm{f})). \tag{15}$$

The projection functionals enforce the constraints when the respective switching functions are active. The functional $y(t, g_y(t))$, which is derived from an equivalent procedure, is function of its own unknown coefficients vector $\boldsymbol{\xi}_y \in \mathbb{R}^m$. The linear mapping

$$z = z_0 + \frac{z_\mathrm{f} - z_0}{t_\mathrm{f} - t_0}(t - t_0) \quad \longleftrightarrow \quad t = t_0 + \frac{t_\mathrm{f} - t_0}{z_\mathrm{f} - z_0}(z - z_0) \tag{16}$$

is necessary to link the domain of definition of the polynomials to the time. Consequently, the n-th order time derivative of the free function for a general coordinate is obtained as [20]

$$\frac{\mathrm{d}^n g(t)}{\mathrm{d}t^n} = \frac{\mathrm{d}^n \boldsymbol{h}^\top}{\mathrm{d}z^n}\,\boldsymbol{\xi}\left(\frac{\mathrm{d}z}{\mathrm{d}t}\right)^n. \tag{17}$$

The two functionals $x(t, g_x(t))$ and $y(t, g_y(t))$ derived above are then substituted in the second order differential equations (Eqs. (1), (4), or (8)) to formulate two nonlinear algebraic expressions $\mathrm{F}_x(t, \boldsymbol{\Xi})$ and $\mathrm{F}_y(t, \boldsymbol{\Xi})$ where $\boldsymbol{\Xi} = [\boldsymbol{\xi}_x^\top; \boldsymbol{\xi}_y^\top]$ is the new vector of unknown coefficients. To estimate the coefficients, the time domain is discretized at some N node points following the Chebyshev–Gauss–Lobatto scheme [15]. This discretization is denser at the boundaries of the domain, which is beneficial when representing the full Earth–Moon transfer and the dynamics is, consequently, more sensitive to small variations at its endpoints. The resulting system of equations is then solved through a root-finding algorithm. This means that the number of nodes is set equal to the number of Chebyshev polynomials employed for the functional interpolation. The resulting system of algebraic equations can be expressed as

$$\mathbb{L}(\boldsymbol{\Xi}) = \begin{Bmatrix} \mathrm{F}_x(t_0, \boldsymbol{\Xi}) \\ \vdots \\ \mathrm{F}_x(t_\mathrm{f}, \boldsymbol{\Xi}) \\ \mathrm{F}_y(t_0, \boldsymbol{\Xi}) \\ \vdots \\ \mathrm{F}_y(t_\mathrm{f}, \boldsymbol{\Xi}) \end{Bmatrix} = \mathbf{0}. \tag{18}$$

A QR algorithm decomposes the Jacobian matrix of the system, and an iterative Newton's method converges to the solution of the root-finding problem within a set tolerance [15].

C. Homotopy continuation

A numerical continuation procedure is a progressive root-finding that, starting from a known seeding solution of a simplified problem, eventually converges to the unknown zero of a more complex, but yet similar, problem. A convex homotopy formulation is expressed as [21]

$$\mathbf{H}(\boldsymbol{\Xi}, \lambda) := (1 - \lambda)\mathbf{G}(\boldsymbol{\Xi}) + \lambda\mathbf{F}(\boldsymbol{\Xi}), \tag{19}$$

where $\boldsymbol{\Xi}$ is the unknown of the problem. The continuation parameter $\lambda \in [0, 1]$ leads to the solution of the non-trivial problem ($\mathbf{H}(\boldsymbol{\Xi}_\mathrm{f}, 1) = \mathbf{0}$) starting from the known zero of the simpler one ($\mathbf{H}(\boldsymbol{\Xi}_0, 0) = \mathbf{0}$). Since Eq. (18) is formulated as $\mathbb{L}(\boldsymbol{\Xi}) : \mathbb{R}^{2\mathrm{N}} \to \mathbb{R}^{2\mathrm{N}}$, one gets that $\mathbf{H}(\boldsymbol{\Xi}, \lambda) : \mathbb{R}^{2\mathrm{N}} \times \mathbb{R} \to \mathbb{R}^{2\mathrm{N}}$. The pseudo-arclength homotopy continuation algorithm attempts to follow the implicitly defined curve $\boldsymbol{c}(s) \in \mathbf{H}^{-1}(\mathbf{0})$ from point $(\boldsymbol{\Xi}_0, 0)$ to $(\boldsymbol{\Xi}_\mathrm{f}, 1)$. The curve, whose points are the zeros of $\mathbf{H}(\boldsymbol{\Xi}, \lambda)$, is parameterized with respect to the arclength s. Differentiating $\mathbf{H}(\boldsymbol{c}(s))$, it results that [11]

$$\mathbf{H}'(\boldsymbol{c}(s))\dot{\boldsymbol{c}}(s) = \mathbf{0} \quad \text{with} \quad \|\dot{\boldsymbol{c}}(s)\| = 1 \tag{20}$$

because of the properties of the arclength. Equation (20) states that the tangent $\dot{\boldsymbol{c}}(s)$ is orthogonal to all rows of the Jacobian matrix $\mathbf{H}'(\boldsymbol{c}(s))$, thereby spanning the one-dimensional kernel $\ker\big(\mathbf{H}'(\boldsymbol{c}(s))\big)$.

The homotopy continuation algorithm traces $\boldsymbol{c}(s)$ until the convergence to the final solution. This can be formulated as the initial value problem

$$\begin{cases} \dot{\boldsymbol{u}} = \dot{\boldsymbol{c}}(s) \\ \boldsymbol{u}_0 = [\boldsymbol{\Xi}_0; 0] \end{cases}. \tag{21}$$

Iteratively, an Euler prediction step $\boldsymbol{u}_{k+1} = \boldsymbol{u}_k + h\dot{\boldsymbol{u}}_k$ with variable step-size h approximates the solution at the next iteration. A Newton-like method based on a QR decomposition corrects the prediction until the condition $\mathbf{H}(\boldsymbol{u}_{k+1}) = \mathbf{0}$ is matched within a certain tolerance [11].

III. Method

In this paper, the generation of Earth–Moon transfers in chaotic dynamic regimes is addressed incrementally. A sequence of steps is performed to gradually refine initial transfer legs until the final convergence to a complete transfer formulated in a high-fidelity dynamic model. A grid search based on the TFC formulation permits to generate a wide range of low-energy transfers. This section describes the procedure and the method practiced in this study.

A. Earth–Moon transfer generation

1. The patched three-body method

A spacecraft can exploit invariant manifolds associated to the Lagrange points to efficiently transit regions in the configuration space, usually at the expenses of longer transfer times [8]. To generate an initial seeding trajectory, invariant manifolds of both the SE-CR3BP and EM-CR3BP are exploited. The preliminary design of an Earth–Moon transfer trajectory can be split into two legs matching in configuration space at an intermediate patching point. Eventually, the full transfer is represented in the EM-BCR4BP. This procedure is enabled by the presence of both an internal and an external regions of prevalence in the EM-BCR4BP, accurately approximating specific sectors of the configuration space of the real dynamics [22]. Firstly, two transfer legs are designed: a departure from a circular Low Earth Orbit (LEO) represented in the SE-CR3BP and an arrival to a Low Lunar Orbit (LLO) whose dynamics adheres to the EM-CR3BP. The two legs are patched at a common point to allow for the continuity in position of the transfer. A small ΔV compensates the slightly different velocity at the patching point [9].

In this work, the spacecraft departs impulsively from a 167 km altitude LEO. Dynamical systems theory suggests that invariant manifolds arise from periodic orbits about Lagrange points. In particular, left and right stable $\mathcal{S}$ and unstable $\mathcal{U}$ invariant manifolds, associated to a certain periodic orbit, can be generated by slightly perturbing the conditions of the latter [23]. An example of L_2 left stable ($\mathcal{S}^{\mathrm{SE}}_{\mathrm{L}_2}$) and unstable ($\mathcal{U}^{\mathrm{SE}}_{\mathrm{L}_2}$) invariant manifolds in the SE-CR3BP is represented in Fig. 3a. The energy of the Lyapunov periodic orbit must be such that its manifolds reach the LEO. The impulsive arrival at a 100 km altitude LLO exploits, at first, the right stable invariant manifold associated to a L_2 Lyapunov orbit in the EM-CR3BP ($\mathcal{S}^{\mathrm{EM}}_{\mathrm{L}_2}$). Its left unstable invariant manifold ($\mathcal{U}^{\mathrm{EM}}_{\mathrm{L}_2}$) then permits to reach the destination orbit. This means that a transit orbit is flown from the outer realm of the system to the inner one. To approach the Moon, the energy of the spacecraft computed in the EM-CR3BP must be just above that of the L_2 point to open the rightmost gate. Moreover, $\mathcal{U}^{\mathrm{EM}}_{\mathrm{L}_2}$ must reach the arrival orbit at the Moon in configuration space so that an impulsive manoeuvre performs the final orbital insertion. Figure 3b shows the tube dynamics related to the arrival leg.

A patching point ensuring the continuity of the entire Earth–Moon transfer in the configuration space must be found. In this work, the arrival leg is generated first, and the departure one is derived consequently. A Poincaré section in the SE-CR3BP at the patching point helps gluing the two dynamic systems. A suitable condition is sought so that forward propagating the states of the spacecraft in the EM-CR3BP, the Moon is approached ballistically. Whereas, the backward propagation in the SE-CR3BP guides the spacecraft back to the Earth [9].

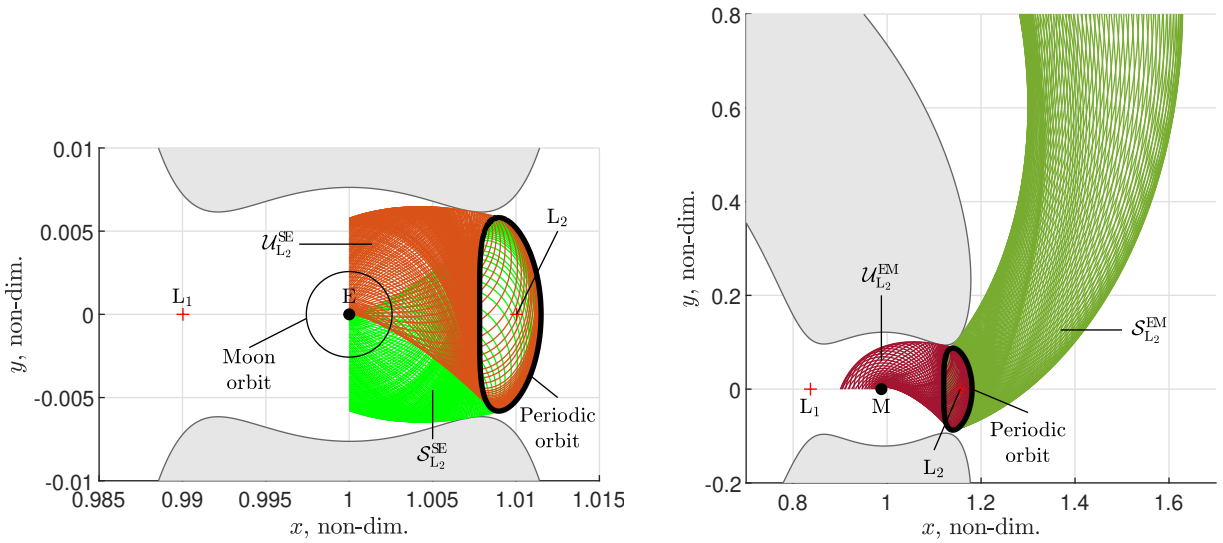

(a) Sun–Earth system, [SErf]. (b) Earth–Moon system, [EMrf].

Fig. 3 Example of tube dynamics of the CR3BPs.

2. Representation in Theory of Functional Connections

TFC functionals are formulated as per Eq. (15) to analytically approximate the two transfer legs previously generated numerically. This representation is then exploited during the continuation and successive design stages.

Considering, for example, the departure leg in the SE-CR3BP system, the trajectory obtained in Sec. III.A.1 serves to estimate the unknown coefficients of $x_{\text{dep}}(t, g_x(t))$ and $y_{\text{dep}}(t, g_y(t))$. Each TFC formulation is constrained at its boundaries to guarantee that the positions at the departure from the Earth and at the patching point are those previously obtained. Likewise, the time of flight (TOF) is preserved. Chebyshev polynomials with a maximum degree of 1000 are employed for the interpolation. A large number of basis functions is indeed necessary to properly approximate the motion of a spacecraft flying in a complex and highly chaotic dynamic environment. The number of basis functions determines the number of discretization points (see Sec. II.B). As pointed out in [17], the basis functions and the supporting functions must be linearly independent. Consequently, a maximum polynomial degree of 1000 entails using 999 Chebyshev polynomials (ranging from degree 2 to 1000) and a corresponding number of points N for discretizing the domain of interest. Cubic splines interpolate the evolution in time of the position, velocity, and acceleration of the leg at the N discretization points. These are fed into a least-squares minimization algorithm, which performs the preliminary estimation of the unknown coefficients $\boldsymbol{\xi}_x^{\text{dep}}$ and $\boldsymbol{\xi}_y^{\text{dep}}$, initially set equal to zero. The two 3N×N Jacobian matrices, one for each spatial coordinate, are computed analytically and decomposed in QR. Eventually, the dynamics is imposed as per Eq. (18) and Newton's method with adaptive step size refines the estimation of the unknown coefficients. This entire procedure is practiced for both legs.

3. Continuation of the legs

The TFC formulation proves to be suitable whenever a continuation procedure is pursued. In this paper, a pseudo-arclength homotopic approach is implemented to refine the two legs into their corresponding more realistic SE-BCR4BP and EM-BCR4BP models. The TFC formulation allows to conserve the initial and final positions, along with the TOF, of each leg, consistently with what obtained in the preceding stages.

The dynamics of the departure leg from the Earth is gradually perturbed by the Moon by multiplying its scaled mass m_{M} in Eq. (5) by the continuation parameter λ. The implicitly defined solution curve $\boldsymbol{c}(s)$ is followed to stretch the solution from complying to the SE-CR3BP dynamics to conform to the full dynamics of the SE-BCR4BP. Equivalently, the arrival leg is continued from the patching point to the LLO. In this case, the scaled mass of the Sun m_S in Eq. (9) is multiplied by the continuation parameter λ, so ensuring a gradual transition from the EM-CR3BP to the EM-BCR4BP. In both cases, the computation of the Jacobian matrices is required. The partial derivatives of the equations with respect to the Chebyshev coefficients and the parameter λ are derived and implemented to enhance the computational efficiency.

4. Final convergence to the transfer trajectory

This last stage performs the final convergence to a full Earth–Moon transfer trajectory in the EM-BCR4BP. In this regard, the departure leg from the LEO must undergo a transformation in order to adhere to the dynamics of the destination model. A final TFC formulation gradually smooths out the intermediate impulse at the patching point, thereby obtaining a pure two-impulse Earth–Moon transfer trajectory.

Firstly, the kinematics of the departure leg is expressed into the EM-BCR4BP model. To perform this transformation, the states of the departure leg at each time instant, as formulated through the TFC representation, are first expressed in the Earth-centered non-rotating reference frame. A scaling is applied to convert the leg in Earth–Moon dimensionless quantities. Finally, a roto-translation is practiced to express the states in the EM-BCR4BP. The transformation requires the knowledge of the Earth–Moon–Sun configuration at each time instant of the departure leg. This procedure generates a curve not strictly satisfying the dynamic equations in Eq. (8). Therefore, two new TFC functionals, one for each position coordinate, are formulated. A least-squares minimization, followed by a root-finding iterative process, leads to the convergence of the departure leg consistently with the dynamics prescribed by the EM-BCR4BP.

A final step is necessary to remove the small impulsive manoeuvre, still present at the patching point, to get a fully ballistic Earth–Moon transfer. Two last TFC functionals are formulated, one for each coordinate. These two pursue the objective of representing the entire transfer by smoothly converging to a trajectory adhering to the dynamics of the EM-BCR4BP, thereby removing the intermediate impulse. The two endpoints are the same departure from the LEO and arrival to the LLO positions previously identified. The TOF is the sum of the two legs durations. A linear combination of Chebyshev polynomials with a maximum degree of 1600 is employed to account for the highly sensitive regions of the phase space. Again, a least-squares approximates the unknown coefficients of the TFC functionals minimizing over the departure and arrival legs, which are now considered as a unique element. A root-finding refines this prediction by imposing the satisfaction of the destination dynamics. The initial conditions, i.e., position and velocity of the spacecraft at the departure from the LEO, obtained after the convergence of the TFC functionals, are numerically propagated to assess the accuracy and reliability of the method.

B. Grid search using the Theory of Functional Connections

A grid search in the EM-BCR4BP over the departure and arrival bi-dimensional positions is performed. The two circular orbits at the endpoints of the transfer are discretized by an angular step of 5° starting from the original departure and arrival positions. The TOF is maintained equal to the transfer duration of the refined trajectory generated in Sec. III.A.4. The initial time, and consequently the Sun angle at the departure from the Earth, is retained fixed as well to reduce the dimensionality of the grid search.

Two TFC functionals are formulated for each combination of departure and arrival positions to represent the constrained time evolution of the spacecraft motion during the Earth–Moon transfer. The unknown coefficients multiplying the Chebyshev polynomials are initialized considering the numerical results obtained after the final convergence in Sec. III.A.4. A root-finding refines this approximation such that the newly obtained transfer trajectory satisfies the dynamics of the EM-BCR4BP. The convergence to a feasible solution is, however, not granted for all combinations of departure and arrival positions. Furthermore, the Chebyshev–Gauss–Lobatto nodes discretizing the transfer are denser at the boundaries. Such a distribution of nodes may be insufficient to guarantee an accurate capture of the dynamics in highly sensitive regions besides the transfer endpoints. To ensure convergence to a feasible transfer, initial conditions obtained through the TFC formulation are propagated numerically. All those transfers crossing the Earth surface are excluded, whereas an event detector halts the propagation upon reaching the destination LLO.

The procedure implemented is expected to streamline the process of generating exterior transfers more effectively. Indeed, the numerical integration of the dynamic equations within a shooting framework is no longer required to converge to a full Earth–Moon transfer trajectory.

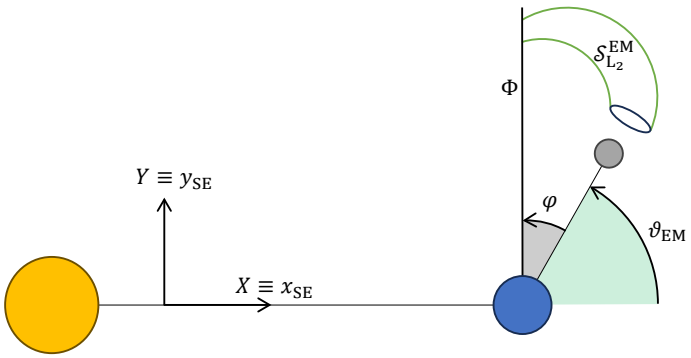

Fig. 4 Earth–Moon–Sun configuration at patching (not to scale). Sun in yellow, Earth in blue, Moon in gray.

IV. Results

The method outlined in Sec. III.A is now applied to design an Earth–Moon transfer complying with the dynamics prescribed by the EM-BCR4BP. Consequently, the grid search described in Sec. III.B is practiced to generate a wide range of admissible low-energy transfers.

A. Exterior transfer trajectory design

1. Transfer legs generation

The design procedure begins with the identification of a suitable energy level for the L_2 Lyapunov orbit in the EM-CR3BP. A Jacobi constant equal to 3.164 164 guarantees the opening of the L_2 gate and generates a left unstable manifold $\mathcal{U}_{L_2}^{EM}$ approaching the destination circular LLO at an altitude of 100 km over the Moon surface. Likewise, a Lyapunov orbit of Jacobi constant equal to 3.000 778 in the Sun–Earth system produces a left stable manifold $\mathcal{S}_{L_2}^{SE}$ reaching the circular 167 km altitude LEO.

$\mathcal{U}_{L_2}^{EM}$ is propagated in the EM-CR3BP system until reaching a horizontal Poincaré section defined at the left side of the Moon ($y = 0$). The crossing with this section generates a one-dimensional curve that is represented in the $(x, \dot{y})$ plane. A suitable transit orbit is obtained if choosing a point inside this curve whose x coordinate equals the destination point on the LLO. The velocity in the x direction can be then readily calculated using Eq. (3).

The patching point between the two legs must be now identified to formalize a proper Earth–Moon–Sun configuration. Without loss of generality, the angle between the rotating frame of the SE-CR3BP and the inertial one is set equal to zero at the time the spacecraft is supposed to be at the patching point. Moreover, the patching point of the two legs is conveniently forced to belong, in configuration space, to a vertical line above the Earth in the Sun–Earth system, as represented in Fig. 4. Therefore, a Poincaré section Φ with coordinates $x = 1 - \mu_{SE}$ and $y > 0$ is introduced in the analysis. Figure 4 depicts the Earth–Moon–Sun instantaneous inertial configuration at the epoch the trajectory switches from the departure leg to the arrival one. The angle θ_{EM} is formed by the Earth-to-Moon direction with respect to the X axis of the inertial frame at the time the spacecraft crosses the Poincaré section. A proper section on the right stable manifold $\mathcal{S}_{L_2}^{EM}$ of the Earth–Moon system, identified by the angle φ, is sought iteratively. The objective is to find the conditions at the section such that a spacecraft would ultimately reach the LLO if its states are propagated forward in the EM-CR3BP, whereas it would approach the LEO if backward propagated in the SE-CR3BP. Numerical experiments demonstrates that a value of $\varphi = 60°$ is an admissible candidate. Figure 5 shows the $(y, \dot{y})$ plane in correspondence of Φ in the Sun–Earth system. To represent $\mathcal{S}_{L_2}^{EM}$ in the figure, a transformation accounting for the instantaneous relative configuration of the three primaries is performed. The conditions at the LLO previously defined are back-propagated in the EM-CR3BP until reaching the patching point, and transformed in the Sun–Earth system. This results in the blue dot in Fig. 5. To guarantee the continuity of the trajectory in the configuration space, the two legs must share the same y coordinate when crossing the section. Moreover, the departure leg must be a non-transit trajectory that exploits a twisting effect to leave the Earth. Therefore, as per [9], the black dot in Fig. 5 must lie outside $\mathcal{U}_{L_2}^{SE}$. The back-propagation in the SE-CR3BP of the states represented by the black dot is then terminated at LEO crossing, thereby generating a suitable departure leg. Figure 6 presents the result of this design in the Sun–Earth system.

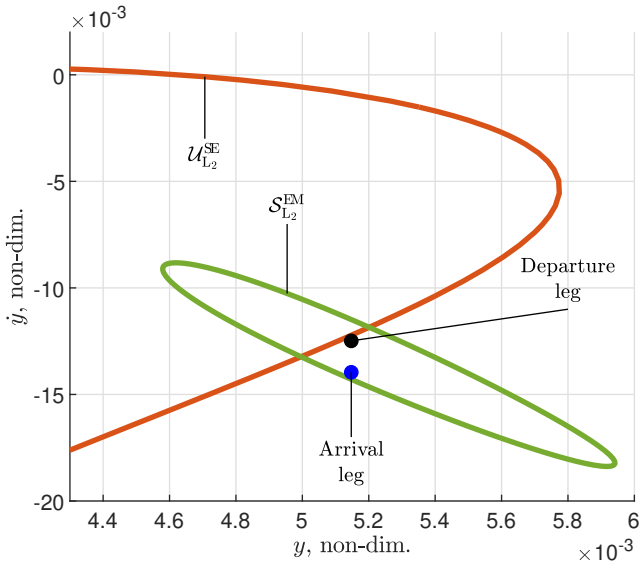

Fig. 5 Poincaré section Φ in Sun–Earth system.

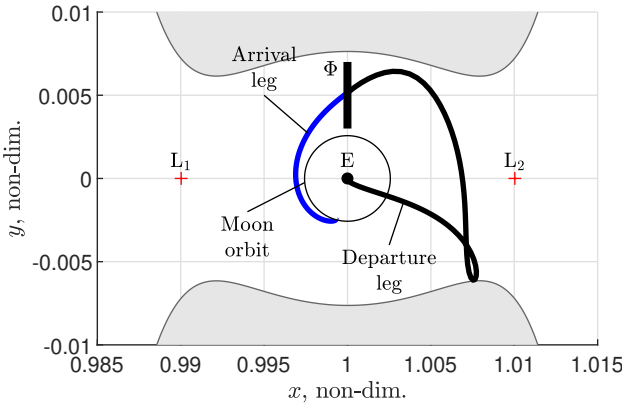

Fig. 6 Transfer legs, [SErf].

2. Theory of Functional Connections formulation and homotopy continuation

Two TFC functionals for each leg are formulated to provide an analytical interpolation of the time evolution of the bi-dimensional position of the spacecraft. As outlined in Sec. III.A.2, a least-squares minimization over the two seeding legs is followed by a root-finding algorithm to estimate the coefficients multiplying the Chebyshev polynomials.

The continuation of the departure leg is presented in Fig. 7a, whereas Fig. 7b shows the gradual refinement of the arrival leg at the Moon. The TOF of each leg is enforced to remain equal to that of the respective seeding one. Hill's regions depicted in the figures are generated over the seeding Jacobi values. The gradual color change from red to black, for the departure leg, and from red to blue for the arrival one, represents the transition in the dynamics. The convergence to the refined departure leg is obtained as a progressive increasing of the perturbation of the Moon, until reaching the dynamics prescribed by the SE-BCR4BP. Similarly, the arrival leg is gradually brought to adhere to the EM-BCR4BP model by introducing the solar perturbation.

3. Final smoothing

A kinematic transformation is applied to the refined departure leg to trace a curve in the Earth–Moon synodic frame. The complying with the dynamics of the EM-BCR4BP is imposed by a TFC formulation. With the two legs now represented in the Earth–Moon system, two last TFC functionals are constructed to connect the constrained departure and arrival points, with a TOF equal to the sum of the durations of the two original legs. A least-squares

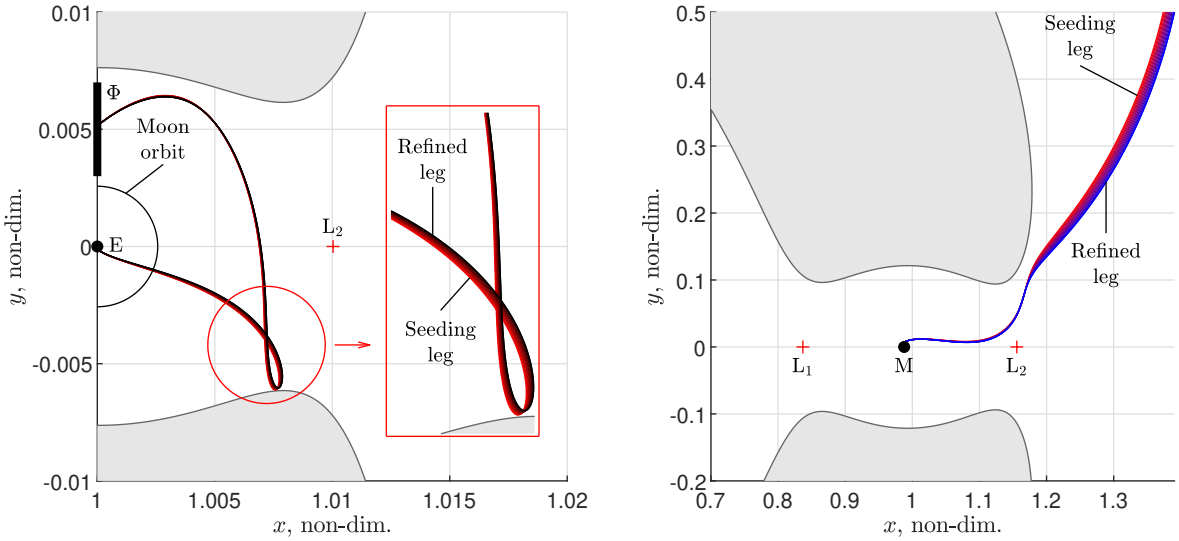

(a) Continuation of departure leg, [SErf].

(b) Continuation of arrival leg, [EMrf].

Fig. 7 Homotopy continuation of transfer seeding legs.

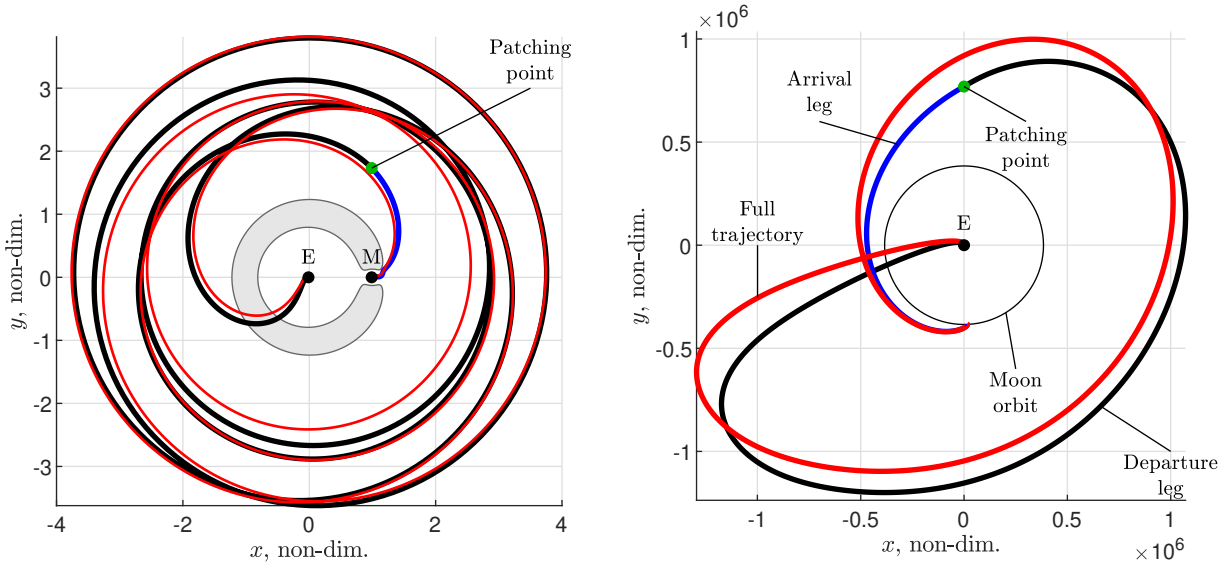

(a) Final trajectory, [EMrf].

(b) Final trajectory, [ECqi].

Fig. 8 Earth–Moon transfer trajectory.

minimization roughly estimates the unknown coefficients, whereas the consequent dynamic imposition makes the convergence to the precise solution approximating the full Earth–Moon transfer. The Newton's algorithm converges in 3.80 seconds[†] after 12 iterations to a norm of the residuals equal to 1×10^{-8}. The intermediate impulsive manoeuvre is smoothed out during the convergence to the full transfer trajectory, as depicted in Fig. 8 in both the synodic and the Earth-centered quasi-inertial (ECqi) frames. Hill's region included in the synodic representation is generated considering the instantaneous Jacobi value at arrival time, equal to 3.151 261. Table 4 reports the initial conditions of the transfer in the Earth–Moon synodic frame, its duration, and costs of the two impulses.

[†] `Matlab`® R2022b, 12th Gen. Intel® Core™ i7-12700, 16.0 GB RAM

Table 4 Transfer trajectory.

Data	Value	Units
x_0	$-1.478\,307\,019 \times 10^{-2}$	-
$\dot{x}_0$	$-1.072\,665\,599 \times 10^{1}$	-
y_0	$1.682\,158\,756 \times 10^{-2}$	-
$\dot{y}_0$	$3.027\,826\,264 \times 10^{-2}$	-
t_0	$-1.102\,775\,345$	-
t_f	$3.616\,627\,242 \times 10^{1}$	-
$\alpha_s^{@t_0}$	1.772 686 870	rad
TOF	162.05	days
ΔV_{dep}	3516.20	ms^{-1}
ΔV_{arr}	660.85	ms^{-1}
ΔV_{tot}	4177.05	ms^{-1}

4. Error analysis

The initial conditions of the transfer trajectory at the LEO are extracted from the TFC functionals and numerically propagated to assess the accuracy of the TFC solution. An event detector at LLO crossing is considered to precisely detect the insertion point. The integration is based on a variable step Runge-Kutta algorithm of orders 7 and 8 with absolute and relative tolerances of 2.5×10^{-14}. Figure 9a depicts the evolution of the TFC position coordinates percent errors, whereas Fig. 9b shows the evolution of the time-synchronized distance between the two trajectories. The red and black vertical lines in Fig. 9a mark the instants when the spacecraft crosses the x and y axes of the EM-BCR4BP frame, respectively. A gradual increase in percent errors is observed. However, it consistently remains bounded below 1.1% even when the trajectory eventually approaches the Moon. Moreover, the maximum planar distance between the trajectory obtained via TFC and numerically propagating the initial conditions reaches a value of 8.60 km.

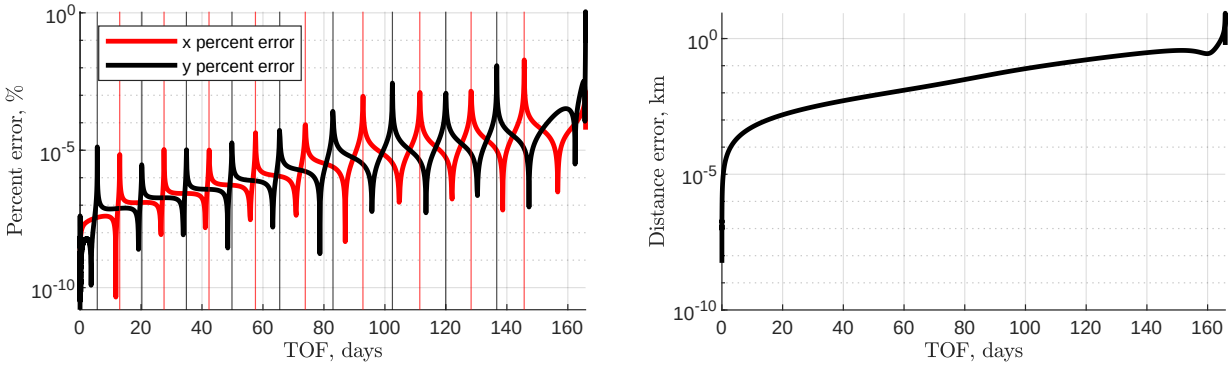

(a) Percent errors, logarithmic scale.

(b) Distance error, logarithmic scale.

Fig. 9 Error analysis.

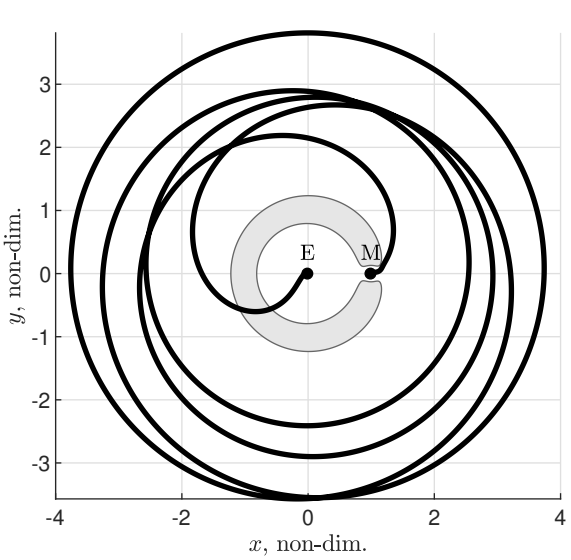

(a) Most efficient transfer, [EMrf].

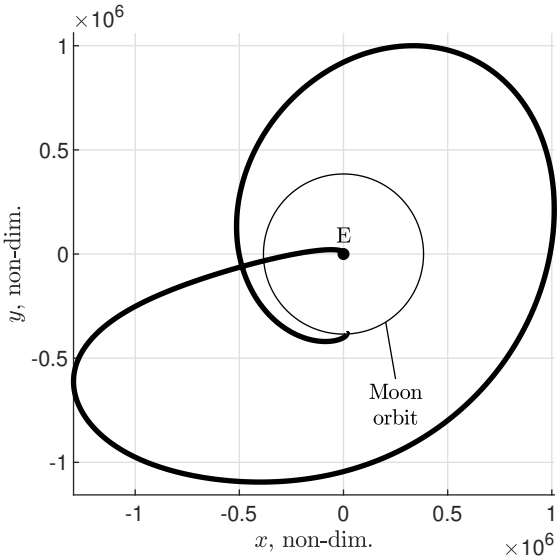

(b) Most efficient transfer, [ECqi].

Fig. 10 Most efficient Earth–Moon transfer after TFC grid search.

Table 5 Most efficient transfer.

Data	Value	Units
x_0	$-8.870\,995\,146 \times 10^{-3}$	-
$\dot{x}_0$	$-1.055\,405\,465 \times 10^{1}$	-
y_0	$1.670\,745\,617 \times 10^{-2}$	-
$\dot{y}_0$	$1.915\,773\,727$	-
t_0	$-1.102\,775\,345$	-
t_f	$3.616\,708\,372 \times 10^{1}$	-
$\alpha_\mathrm{s}^{@t_0}$	$1.772\,686\,870$	rad
TOF	162.05	days
ΔV_dep	3201.88	ms^{-1}
ΔV_arr	638.44	ms^{-1}
ΔV_tot	3840.32	ms^{-1}

B. Earth–Moon grid search

The procedure outlined in Sec. III.B is now employed to automatically generate a large number of Earth–Moon transfer trajectories in the EM-BCR4BP system. Exploiting the TFC formulation, several full low-energy exterior transfers result from the grid search over the departure and arrival positions. The initial conditions of each converged solution are numerically propagated to ensure the accuracy of the results. As before, an event detector precisely identifies the LLO insertion. Overall, approximately 2300 compliant trajectories are obtained, the best of which features a total cost of 3840.32 ms^{-1} and a TOF of 162.05 days. Figure 10 plots this solution in both the synodic and the quasi-inertial frames, whereas Table 5 summarizes its initial conditions and performances. Hill's region depicted in the figure is computed over the energy at the arrival time.

V. Conclusion

This work presents a novel methodology to design two-impulse, long-duration, low-energy trajectories in multibody dynamic environments. Firstly, two legs are generated to approximate an Earth–Moon transfer patching two planar circular restricted three-body problems. A homotopic continuation process is implemented to gradually stretch the two legs. The analytical formulation of the legs in Theory of Functional Connections (TFC) ensures a smooth and precise convergence towards more dynamically rich models. Eventually, the full two-impulse Earth–Moon transfer adheres to the planar Earth–Moon Sun-perturbed, bi-circular restricted four-body problem dynamic model. A grid search over position points belonging to the departure and arrival circular orbits is performed to generate several trajectories.

The TFC proves suitable to generate exterior Earth–Moon transfers leveraging the perturbation of the Sun, despite the chaoticity of the models. The representation in TFC is particularly convenient anytime the solution must be refined into a more complex problem. Therefore, its synergy with a homotopic continuation procedure is demonstrated. The results show that this approach is successful in refining trajectories into higher-fidelity dynamic models. Moreover, the TFC provides a favorable formulation to generate a multitude of admissible low-energy transfer trajectories that directly connect the departure and destination orbits. Unlike similar works, the grid search generates compliant trajectories circumventing the need of numerically propagating the dynamic equations within a shooting framework.

Acknowledgments

The authors would like to thank Professor D. Mortari and Dr. A. K. de Almeida Jr. for the interesting discussion regarding the TFC. Moreover, the authors acknowledge the support received by Dr. C. Giordano for the numerical implementation of the Chebyshev polynomials.

References

[1] Cheetham, B., "Cislunar Autonomous Positioning System Technology Operations and Navigation Experiment (CAPSTONE)," *ASCEND 2021*, American Institute of Aeronautics and Astronautics, 2021. https://doi.org/10.2514/6.2021-4128.

[2] Di Tana, V., Cotugno, B., Simonetti, S., Mascetti, G., Scorzafava, E., and Pirrotta, S., "ArgoMoon: There is a Nano-Eyewitness on the SLS," *IEEE Aerospace and Electronic Systems Magazine*, Vol. 34, No. 4, 2019, pp. 30–36. https://doi.org/10.1109/MAES.2019.2911138.

[3] Funase, R., Ikari, S., Miyoshi, K., Kawabata, Y., Nakajima, S., Nomura, S., Funabiki, N., Ishikawa, A., Kakihara, K., Matsushita, S., Takahashi, R., Yanagida, K., Mori, D., Murata, Y., Shibukawa, T., Suzumoto, R., Fujiwara, M., Tomita, K., Aohama, H., Iiyama, K., Ishiwata, S., Kondo, H., Mikuriya, W., Seki, H., Koizumi, H., Asakawa, J., Nishii, K., Hattori, A., Saito, Y., Kikuchi, K., Kobayashi, Y., Tomiki, A., Torii, W., Ito, T., Campagnola, S., Ozaki, N., Baresi, N., Yoshikawa, I., Yoshioka, K., Kuwabara, M., Hikida, R., Arao, S., Abe, S., Yanagisawa, M., Fuse, R., Masuda, Y., Yano, H., Hirai, T., Arai, K., Jitsukawa, R., Ishioka, E., Nakano, H., Ikenaga, T., and Hashimoto, T., "Mission to Earth–Moon Lagrange Point by a 6U CubeSat: EQUULEUS," *IEEE Aerospace and Electronic Systems Magazine*, Vol. 35, No. 3, 2020, pp. 30–44. https://doi.org/10.1109/MAES.2019.2955577.

[4] Topputo, F., Merisio, G., Franzese, V., Giordano, C., Massari, M., Pilato, G., Labate, D., Cervone, A., Speretta, S., Menicucci, A., Turan, E., Bertels, E., Vennekens, J., Walker, R., and Koschny, D., "Meteoroids detection with the LUMIO lunar CubeSat," *Icarus*, Vol. 389, 2023, p. 115213. https://doi.org/10.1016/j.icarus.2022.115213.

[5] Smith, M., Craig, D., Herrmann, N., Mahoney, E., Krezel, J., McIntyre, N., and Goodliff, K., "The Artemis program: an overview of NASA's activities to return humans to the Moon," *2020 IEEE Aerospace Conference*, IEEE, 2020. https://doi.org/10.1109/AERO47225.2020.9172323.

[6] Topputo, F., Vasile, M., and Bernelli-Zazzera, F., "Low Energy Interplanetary Transfers Exploiting Invariant Manifolds of the Restricted Three-Body Problem," *The Journal of the Astronautical Sciences*, Vol. 53, No. 4, 2005, pp. 353–372. https://doi.org/10.1007/bf03546358.

[7] Doedel, E. J., Romanov, V. A., Paffenroth, R. C., Keller, H. B., Dichmann, D. J., Galán-Vioque, J., and Vanderbauwhede, A., "Elemental Periodic Orbits Associated with the Libration Points in the Circular Restricted 3-Body Problem," *International Journal of Bifurcation and Chaos*, Vol. 17, No. 08, 2007, pp. 2625–2677. https://doi.org/10.1142/s0218127407018671.

[8] Oshima, K., Topputo, F., and Yanao, T., "Low-energy transfers to the Moon with long transfer time," *Celestial Mechanics and Dynamical Astronomy*, Vol. 131, No. 1, 2019. https://doi.org/10.1007/s10569-019-9883-7.

[9] Koon, W. S., Lo, M. W., Marsden, J. E., and Ross, S. D., "Low Energy Transfer to the Moon," *Celestial Mechanics and Dynamical Astronomy*, Vol. 81, No. 1/2, 2001, pp. 63–73. https://doi.org/10.1023/a:1013359120468.

[10] Mortari, D., "The Theory of Connections: Connecting Points," *Mathematics*, Vol. 5, No. 4, 2017, p. 57. https://doi.org/10.3390/math5040057.

[11] Allgower, E. L., and Georg, K., *Introduction to Numerical Continuation Methods*, Society for Industrial and Applied Mathematics, 2003. https://doi.org/10.1137/1.9780898719154.

[12] Szebehely, V., *Theory of Orbit*, Elsevier, 1967. https://doi.org/10.1016/b978-0-12-395732-0.x5001-6.

[13] Koon, W. S., Lo, M. W., Marsden, J. E., and Ross, S. D., "Dynamical Systems, the Three-Body Problem and Space Mission Design," *Equadiff 99*, World Scientific Publishing Company, 2000, pp. 1167–1181. https://doi.org/10.1142/9789812792617_0222.

[14] Topputo, F., "On optimal two-impulse Earth–Moon transfers in a four-body model," *Celestial Mechanics and Dynamical Astronomy*, Vol. 117, No. 3, 2013, pp. 279–313. https://doi.org/10.1007/s10569-013-9513-8.

[15] Boyd, J. P., *Chebyshev and Fourier spectral methods*, Dover Publications, 2001.

[16] Mortari, D., "Least-Squares Solution of Linear Differential Equations," *Mathematics*, Vol. 5, No. 4, 2017, p. 48. https://doi.org/10.3390/math5040048.

[17] Mortari, D., Johnston, H., and Smith, L., "High accuracy least-squares solutions of nonlinear differential equations," *Journal of Computational and Applied Mathematics*, Vol. 352, 2019, pp. 293–307. https://doi.org/10.1016/j.cam.2018.12.007.

[18] Leake, C., Johnston, H., and Mortari, D., "The Multivariate Theory of Functional Connections: Theory, Proofs, and Application in Partial Differential Equations," *Mathematics*, Vol. 8, No. 8, 2020, p. 1303. https://doi.org/10.3390/math8081303.

[19] Johnston, H., Lo, M. W., and Mortari, D., "A Functional Interpolation Approach to Compute Periodic Orbits in the Circular-Restricted Three-Body Problem," *Mathematics*, Vol. 9, No. 11, 2021, p. 1210. https://doi.org/10.3390/math9111210.

[20] de Almeida Junior, A. K., Johnston, H., Leake, C., and Mortari, D., "Fast 2-impulse non-Keplerian orbit transfer using the Theory of Functional Connections," *The European Physical Journal Plus*, Vol. 136, No. 2, 2021. https://doi.org/10.1140/epjp/s13360-021-01151-2.

[21] Wang, Y., and Topputo, F., "A TFC-based homotopy continuation algorithm with application to dynamics and control problems," *Journal of Computational and Applied Mathematics*, Vol. 401, 2022, p. 113777. https://doi.org/10.1016/j.cam.2021.113777.

[22] Castelli, R., "On the Relation Between the Bicircular Model and the Coupled Circular Restricted Three-Body Problem Approximation," *Nonlinear and Complex Dynamics*, Springer New York, 2011, pp. 53–68. https://doi.org/10.1007/978-1-4614-0231-2_4.

[23] Koon, W. S., Lo, M. W., Marsden, J. E., and Ross, S. D., *Dynamical Systems, the Three-Body Problem and Space Mission Design*, Marsden Books, 2011.